Bulletin of the Seismological Society of America, 90, 6B, pp. S77–S94, December 2000

Site Amplification in the Los Angeles Basin from Three-Dimensional Modeling of Ground Motion

by K. B. Olsen

Abstract It is well established that sedimentary basins can significantly amplify earthquake ground motion. However, the amplification at any given site can vary with earthquake location. To account for basin response in probabilistic seismic hazard analysis, therefore, we need to know the average amplification and intrinsic variability (standard deviation) at each site, given all earthquakes of concern in the region. Due to a dearth of empirical ground-motion observations, theoretical simulations constitute our best hope of addressing this issue. Here, 0–0.5 Hz finite-difference, finite-fault simulations are used to estimate the three-dimensional (3D) response of the Los Angeles basin to nine different earthquake scenarios. Amplification is quantified as the peak velocity obtained from the 3D simulation divided by that predicted using a regional one-dimensional (1D) crustal model. Average amplification factors are up to a factor of 4, with the values from individual scenarios typically differing by as much as a factor of 2.5. The average amplification correlates with basin depth, with values near unity at sites above sediments with thickness less than 2 km, and up to factors near 6 above the deepest ($\approx$ 9 km) and steepest-dipping parts of the basin. There is also some indication that amplification factors are greater for events located farther from the basin edge. If the 3D amplification factors are divided by the 1D vertical *SH*-wave amplification below each site, they are lowered by up to a factor of 1.7. The duration of shaking in the 3D model is found to be longer, by up to more than 60 seconds, relative to the 1D basin response. The simulation of the 1994 Northridge earthquake reproduces recorded 0–0.5 Hz particle velocities relatively well, in particular at near-source stations. The synthetic and observed peak velocities agree within a factor of two and the log standard deviation of the residuals is 0.36. This is a reduction of 54% and 51% compared to the values obtained for the regional 1D model and a 1D model defined by the velocity and density profile below a site in the middle of the basin (DOW), respectively. This result suggests that long-period ground-motion estimation can be improved considerably by including the 3D basin structure. However, there are uncertainties concerning accuracy of the basin model, model resolution, the omission of material with shear velocities lower than 1 km/s, and the fact that only nine scenarios have been considered. Therefore, the amplification factors reported here should be used with caution until they can be further tested against observations. However, the results do serve as a guide to what should be expected, particularly with respect to increased amplification factors at sites located above the deeper parts of the basin.

Introduction

The metropolitan area of the greater Los Angeles area is underlain by a deep sedimentary basin. Ground motions in such basins can be significantly amplified, as was the case in Mexico City during the 1985 M_u 8.1 Michoacan earthquake, and in the South Bay of San Francisco during the 1989 **M** 7 Loma Prieta event. This study explores ground-motion amplification of seismic waves due to the deep LA basin.

Ground-motion simulations in elastic media that include complicated 2D or 3D velocity structures, even for simplified source implementations such as plane waves (e.g., Frankel and Vidale, 1992; Olsen and Schuster, 1995; Olsen *et al.,* 1995a) or line/point sources (e.g., Yomogida and Etgen, 1993; Scholler *et al.,* 1994; Graves, 1995) have shown significant basin effects. These results were further consolidated

by the first ground motion simulations including both the 3D basin structure and the finite-fault source effects (Frankel, 1993; Olsen *et al.,* 1995b; Olsen and Archuleta 1996). While all of the 3D studies have been limited to low frequencies ($\lesssim$1 Hz) or very limited spatial volume, due to extensive computational requirements, they all demonstrated significant 3D effects from the basin structures. These effects include the generation of surface waves at the basin edges, and a strong correlation between the duration of shaking and the site location within the basin. Such correlation suggests that the accuracy of long-period attenuation relations may be improved by including the amplification effects of sedimentary basins. For the purposes of probabilistic seismic hazard analysis, we need to know the average amplification factor at each site for all sources of concern throughout the region, as well as the intrinsic variability of the response with respect to the different earthquake locations. Given a lack of observations, the response of the Los Angeles basin is explored numerically using the Southern California Earthquake Center (version 1) 3D velocity model (Magistrale *et al.,* 1998) and a regional 1D rock model (Hadley and Kanamori, 1977). Nine different earthquake scenarios are considered, including two large earthquakes on the San Andreas fault and seven moderate-sized earthquakes on the Los Angeles fault system. The scenarios use variable slip distributions and rise times related to the magnitude. These scenarios are intended to reflect some of the variability of basin response for all sources of concern in the region. From the simulations, I compute 3D/1D ratios of peak velocities and 3D-1D differences of durations. The kinematic earthquake rupture (Olsen and Archuleta, 1996) and viscoelastic wave propagation (Robertsson *et al.,* 1994; Blanch *et al.,* 1995) are numerically modeled using a 3D finite-difference method.

This article is divided into the following parts. After the introduction, the LA basin models and earthquake scenarios are described. The following section describes the finite-difference scheme and the finite-fault source implementation used in the simulations. The Los Angeles basin amplification is then presented, including the response to 1D vertical SH waves, amplification maps for the nine scenarios and their average, correlation of the amplification with basin depth, and the basin effects on durations. Finally I discuss the accuracy and limitations of the basin amplification results, including comparison of the amplification results to data from the Northridge earthquake. For a discussion of the wave propagation using synthetic seismograms and snapshots, see the Appendix.

Description of the Earth Models and Scenario Earthquakes

Basin Models

In order to compute both 3D and 1D ground motions, I use two elastic models of the Los Angeles area: a 3D model assembled by Magistrale *et al.* (1998) (M3D), and the 1D regional model given by Hadley and Kanamori (1977) (HK1D). Outside the 3D basin structures the models are identical. The spatial resolution of the model is approximately 0.5 km (H. Magistrale, written comm., 1995). Within the basins, the *P*-wave velocity is determined from the depths and ages estimated for four geological horizons (Faust, 1951) and calibrated with local *P*-wave velocity models for the basins. The density is estimated from the *P*-wave velocity using the Nafe-Drake relation (Nafe and Drake, 1960). The density is used to find Poisson's ratio using the relation of Ludwig *et al.* (1970). Finally, the *S*-wave velocity is computed from the *P*-wave velocity and Poisson's ratio. Although surficial sediments have lower velocities, numerical considerations impose a minimum *S*-wave velocity of 1.0 km/sec at the earth's surface. The corresponding *P*-wave velocity is 2.4 km/sec.

Figure 1 shows a topographic map of southern California. The larger rectangular area depicts the extent of the model for the San Andreas Fault (SAF) scenarios. The smaller rectangle shows the region used for modeling the remaining scenarios, which is further shown in Figure 2 including the surface projections of the fault planes associated with the earthquake scenarios. Note that the reference frame of the model in Figure 2 is rotated 28° counterclockwise from North to minimize the computational requirements for the simulations. The axis of the main basin trends approximately 118°, as does the San Andreas fault. Throughout this article, I use azimuths of 118° and 28° to analyze the horizontal ground motion for the earthquake simulations. The

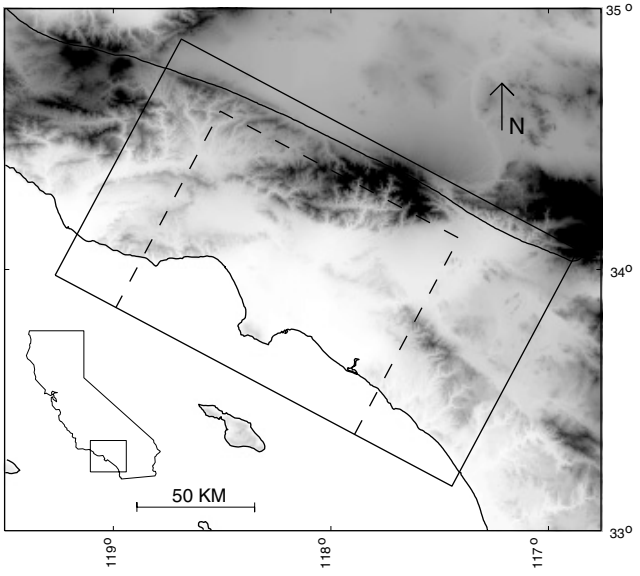

Figure 1. Topographic map of southern California centered on the Los Angeles region. The dashed rectangle shows the areal extent of the basin model used in this study. The area within the solid rectangle was used for the SAF scenarios. Also shown is the trace of the San Andreas fault.

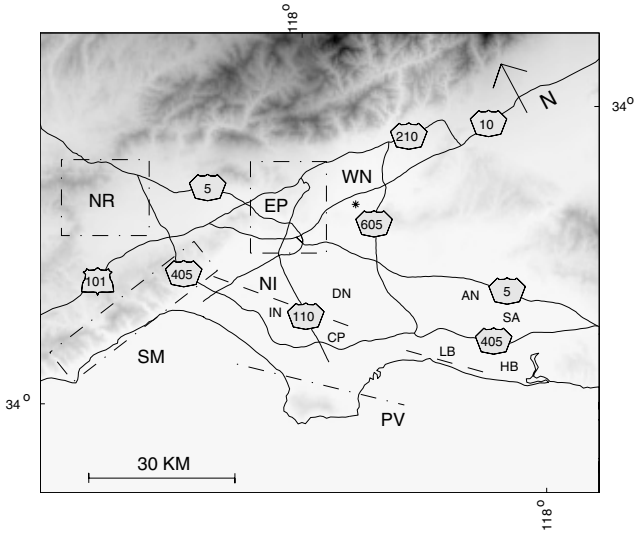

Figure 2. Topographic map of the Los Angeles area model. The dash-dot lines show the surface projections of faults where I have simulated ruptures in this study: Palos Verdes (PV), Elysian Park (EP), Santa Monica (SM), Newport-Inglewood (NI), and the faults that ruptured during the 1994 **M** 6.7 Northridge (NR), the 1933 **M** 6.4 Long Beach (LB), and the 1987 **M** 5.9 Whittier-Narrows (WN) events. The thin solid lines depict major freeways in the modeling area. AN, Anaheim; CP, Compton; DN, Downey; HB, Huntington Beach; IN, Inglewood; and SA, Santa Ana.

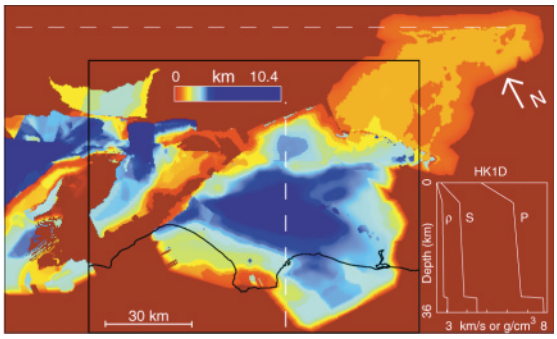

Figure 3. 3D image of the isosurface for an *S*-wave velocity of 2.5 km/sec for the area within the large rectangle shown in Figure 1. The northwest-southeast trending dashed white line is my approximation of the SAF trace. The northeast-southwest trending dashed white line is a profile used to display synthetic seismograms (see Appendix). The black rectangle shows the area used for the amplification study in this article. The thick black contour is the coastline. The 1D regional model (HK1D) is shown in the lower right corner.

3D nature of the model is characterized in Figure 3 by an isosurface corresponding to an *S*-wave velocity of 2.5 km/s. The large depression is the Los Angeles basin. The smaller basin to the northwest is located below the San Fernando Valley (SFV), separated from the Los Angeles basin by the Santa Monica Mountains, with the Ventura basin continuing to the North. A relatively small basin is located below the San Gabriel Valley (SGV), and the larger, but shallower Chino basin extends the LA basin to the East. Finally, the San Bernardino basin continues the Chino basin toward the east to the SAF. The 1D regional model (HK1D) is shown as an inset in Figure 3. The topography above sea level is not included in the simulations.

Earthquake Scenarios

I have selected nine scenario earthquakes to calculate the basin amplification, namely a bilateral strike-slip rupture on the Palos Verdes fault (PV), blind thrust on the Elysian Park fault (EP), thrust on the Santa Monica fault (SM), southeast (SAFN) and northwest (SAFS) propagating ruptures on a 170 km-long stretch of the SAF, northwest propagating rupture on the Newport-Inglewood fault (NI), and approximations of the 1994 **M** 6.7 Northridge (NR), 1933 **M** 6.4 Long Beach (LB), and 1987 **M** 5.9 Whittier-Narrows (WN) earthquakes (Fig. 2, Table 1). These earthquakes are all within the "geological reasonable scenarios" defined by Dolan *et al.* (1995).

Finite-Difference Modeling

The physical model is discretized with a grid spacing equivalent to 5 nodes per minimum shear wavelength of 2.5 km, the rule-of-thumb commonly used for fourth-order schemes (e.g., Levander, 1988) which limits the maximum resolved frequency to 0.5 Hz. The full model is discretized at 0.4 km spacing into 10–24 million grid points, dependent on the earthquake scenario. Absorbing boundary conditions (Clayton and Engquist, 1977) are applied to the sides of the computational model. To further reduce artificial reflections the boundaries of the model are padded with a zone of attenuative material (Cerjan *et al.,* 1985). The 3D modeling parameters are listed in Table 2. All scenarios are kinematically simulated using variable slip distributions, radially propagating outward with a constant rupture velocity. I used a rupture velocity of 2.7 km/s for the SAF scenarios and 3 km/s for all other finite-fault scenarios in this study. The slip distributions (Fig. 4) are taken as variations of the kinematic inversion results for the 1992 Landers (Wald and Heaton, 1994) and 1994 Northridge (Wald *et al.,* 1996, combined result) events. I use a triangular slip rate function in the 3D simulations. The rise time is 3 sec for the SAF ruptures, 0.2 sec for the Whittier Narrows earthquake, and 1 sec for all remaining scenarios. The source is implemented in the finite-difference grid by adding $-M_{ij}(t)/V$ to $S_{ij}(t)$ where $M_{ij}(t)$ is the ijth component of the moment tensor for the earthquake, $V = dx^3$ is the cell volume, and $S_{ij}(t)$ is the ijth component of the stress tensor on the fault at time t. The synthetic seis-

Table 1
Earthquake Rupture Parameters

	Hypocenter Longitude, Latitude, Depth (km)	Fault Width, Length, Depth to Top (km)	Dip	Strike	Rake	Moment Magnitude
EP	−118.205, 34.102, 14.8	21, 16, 10.5	25	298	90	6.75
SM	−118.643, 34.065, 10.4	17, 37, 0.4	65	260	90	6.75
NR	−118.53, 34.205, 17.6	24, 18, 5.0	40	118	101	6.7
PV	−118.332, 33.781, 7.2	16, 35, 0.4	90	141	180	6.75
SAFN	−118.657, 34.79, 4.0	16, 170, 0.4	90	118	180	7.5
WN	−118.072, 34.049, 14.4	0.4, 0.4, 7.0	27	270	90	5.9
SAFS	−117.088, 34.095, 15.2	16, 170, 0.4	90	118	180	7.5
LB	−117.99, 33.655, 9.6	10, 18, 0.4	90	133	180	6.4
NI	−118.237, 33.885, 7.6	15, 41, 0.4	90	138	180	6.75

Table 2
3-D Modeling Parameters

Spatial discretization (km)	0.4
Temporal discretization (sec)	.025
Lowest *P*-wave velocity (km/sec)	2.41
Lowest *S*-wave velocity (km/sec)	1.0
Lowest density (kg/m^3)	2070
Number of timesteps	3600–5000
Simulation time (sec)	90–125

mograms are lowpass filtered to frequencies less than 0.5 Hz (Butterworth filter with 4 poles and 2 passes). I use a staggered-grid finite-difference scheme to solve the 3D elastic equations of motion (Levander, 1988; Graves, 1996); the accuracy is fourth-order in space and second-order in time. The numerical implementation of the 3D scheme is described in Olsen (1994). Viscoelasticity is implemented using stress relaxation independently for *P* and *S* waves (Robertsson *et al.,* 1994; Blanch *et al.,* 1995) using a standard linear solid model with one relaxation peak. The accuracy, relative to a frequency independent of the attenuation model, of the smallest Q in the model, $Q_s = 100$, is estimated to be less than about 5% for the central 1/3 of the bandwidth of interest (see Blanch *et al.,* 1995; Fig. 4). There are essentially no constraints on the values of Q for the area of interest, and no well-established relation between Q and velocity is available. I assumed that $Q_s = 0.1\ V_s$ (m/s) and $Q_p = 1.5\ Q_s$ which, to my knowledge, is commonly used in absence of better constraints on Q.

Los Angeles Basin Amplification

I use ratios of 0–0.5 Hz horizontal peak velocities for the 3D and 1D models throughout the 115 km by 95 km area shown in Figures 1 and 2. The 3D/1D ratios have the advantage of eliminating the geometrical spreading effects included in the 3D response and the 1D reference value for a given site. The conventional corrections for such effects using $1/r$ attenuation for body-wave propagation can be misleading for traces that include strong surface waves. A disadvantage of the method is that artifacts may show up in the amplification maps due to singularities in the rupture pattern. However, such effects are found to be small for the scenarios in this study. In this section I emphasize the amplification patterns for the scenarios, and the wave propagation underlying the amplification is discussed more rigorously in the Appendix.

1D Vertical SH-wave Amplification

The amplification observed above the Los Angeles basin is only partly controlled by the 3D basin structure. Another contribution to the amplification arises from the differences in velocities and densities between the two models in the area where the basin is located (lowest *S*-wave velocity is 2.7 km/s for the 1D model, 1.0 km/s for the 3D model). To estimate the latter contribution I carried out a series of 1D simulations where the models were given by the velocity and density profiles of the 3D model (hereafter referred to as the 1D vertical *SH*-wave amplification). The source was a vertically incident plane *SH* wave with an isosceles triangular slip rate function and a rise time of 1 sec, and the response was computed using a finite-difference method. The 0–0.5 Hz 1D vertical *SH*-wave amplification, relative to that at a site in the background model, are shown in Figure 5. These ratios reflect the amplification due to the lower impedance for vertically propagating *SH* waves in the 3D basin. The ratios are controlled by the variation of the impedance within the basin and the smoothing effect of the bandwidth of the source-time function. The largest peak velocity amplification factor due to the differences in impedance is about 1.7 obtained above large parts of the basin. In the following I will use the 1D vertical *SH*-wave amplification to separate the amplification due to the 3D basin structure from the total amplification.

Scenario Amplification Maps

Figure 6 shows 3D/1D amplification values for the nine earthquake scenarios described previously, corrected for the 1D vertical *SH*-wave amplification. Note that both the pattern and amplitudes of the amplification distributions for the nine scenarios vary considerably within the model area. While the deeper basin areas are generally characterized by

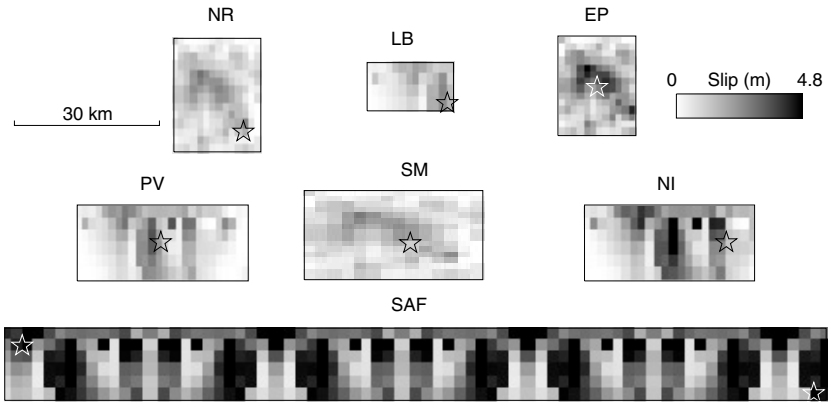

Figure 4. Variable slip distributions for the nine earthquake scenarios. The stars depict the hypocenters in the simulations.

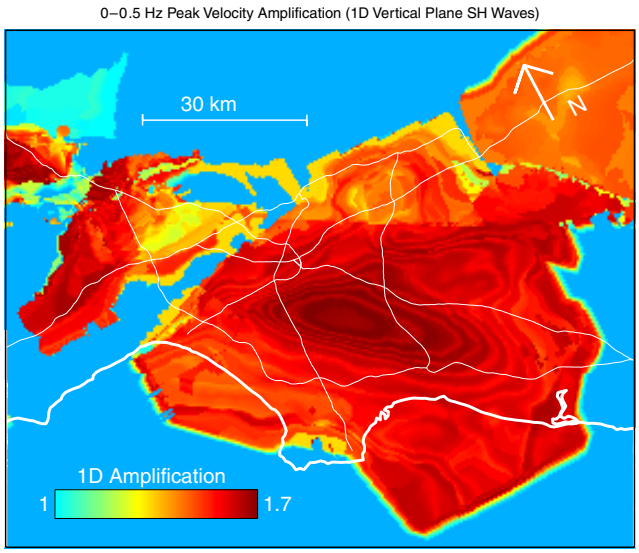

Figure 5. Image of 0–0.5 Hz peak velocities for a series of 1D simulations, normalized to the value in rock. The models used in the simulations are the 1D velocity and density profiles directly below each site in the 3D basin model, and the source for the simulations is a vertically incident *SH* wave with a rise time of 1 sec. The thick line is the coastline and the thin solid lines depict major freeways in the modeling area.

increased 3D/1D ratios, some of the largest amplification tends to occur above the most steeply-dipping basin boundaries and the basin edges, similar to the results by Olsen *et al.* (1995a) for the Salt Lake Basin. This amplification is typically caused by the generation of surface waves at the basin edges, along with resonance in shallower sub-basins such as the SGV (see Appendix).

The largest basin amplification is obtained for the EP (11.2), NR (10.8) and SAFS (8.1) events (Figure 6). Compared to PV, EP, LB, NI, SM, and WN, the NR and SAF from southeast and to a lesser extent, the SAFN generate generally larger amplification above the basin. This pattern suggests that the amplification increases with distance from the causative fault to the basin structure. A possible reason for this pattern is that the larger-amplitude surface waves generated for the distant events, in part at the basin edges (see Appendix), are more prone to amplification than are the predominant body waves impinging onto the basin sediments from the nearby earthquakes. This interpretation is supported by evidence from the variability of Northridge aftershock ground motions in the San Fernando Valley (Hough *et al.*, 1995).

Mean LA Basin Amplification

In order to construct an amplification map for Los Angeles that combines the variations in fault location and rupture mechanism, I have calculated the mean 0–0.5 Hz peak velocity ratios with and without correction for the 1D vertical *SH*-wave amplification. The average, maximum values, and the standard deviation for the nine earthquake scenarios described above are shown in Figure 7. The LA and SGV basins generally show mean amplification above 3, with localized areas above 4. While some of the largest mean amplification occurs above the deepest part of the basin, considerable mean amplification (>3.5) is found near the eastern and western edges of the LA basin as well as in the SGV. The overall largest amplifications (up to 11.2) and 18.5 with and without correction for 1D vertical *SH*-wave amplification, respectively) occur near Palos Verdes, Inglewood, and Santa Ana and Anaheim. The estimated standard deviation (of the natural-log amplification) shows generally lower values for larger mean amplification. For example, the standard deviation is less than 0.8 at most sites where the total mean amplification is larger than 3. The largest uncertainties above the basin are found on Palos Verdes, in the southern SFV, and northwest of SFV. The large uncertainty in the southern SFV is due to strong amplification in this area from NR, PV, and SAFN. Finally, the large uncertainty in the southern part of and to the northwest of SFV is due to relative large amplification from SAFS.

Note, that the variation in the 3D mean basin amplification is in part controlled by the azimuth of the incident waves. For example, the largest amplification due to the

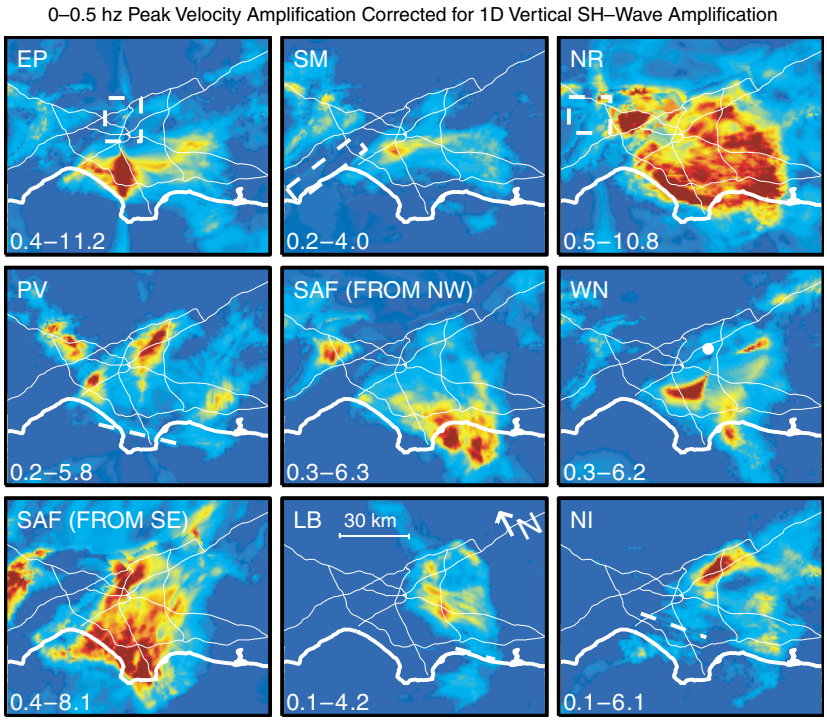

Figure 6. Maps of 3D/1D 0–0.5 Hz peak velocity ratios for nine scenarios (see Figures 1 and 2), divided by the 1D vertical *SH*-wave amplification (Figure 5). The thin white lines show major freeways in the Los Angeles area. The thick white line is the coastline. The range of amplification values is listed for each scenario.

SAFN occurs in the southern end of the basin, while that for the SAFS occurs in the western parts. This pattern is due to reflections from the basin boundaries and surface wave generation at the edges. For more discussion of the wave propagation of the individual scenarios, see the Appendix.

Amplification Versus Basin Depth

Another way of characterizing the basin amplification is to average values for sites located above similar velocity/density profiles in the basin. Here I choose to average the values for sites with common depth to the isosurface of 2.5 km/sec. Figure 8 shows these values for the nine scenario earthquakes as well as the mean and log standard deviation. I have omitted values for depths larger than 6 km due to their limited number. I have also omitted values for a small area of Cretateous outcrops in the vicinity of the SFV where the velocities may be overestimated (Magistrale, personal comm., 1999). The amplification generally increases gradually with increasing depth to the isosurface. However, exceptions are SAFS and NR, which both show average amplification of up to about 3 for sites with depths less than 2 km. These shallow basin sites are distributed fairly evenly along all edges of the basins within the model, and the increased shallow amplification for the two scenarios is caused by surface wave generation and resonance (see Appendix). The NR scenario is also responsible for the largest amplification values (up to about 6.5), as noted from the scenario amplification maps. The least amplification with depth is obtained for the NI, LB, and PV scenarios. In fact, these and other scenarios generate deamplification at shallow basin sites, caused by the transfer of energy from the initial arrivals to secondary phases in the 3D model (see Appendix). The mean amplification values for the scenarios as a function of depth to the isosurface gradually increase from 1 outside the basin to about 3.3 above the deepest part of the basin. Figure 9 shows the values from Figure 8, divided by the 1D vertical *SH*-wave amplification (Figure 5). These corrected amplification factors are less than about a factor of 4, largest above the deepest part of the basin. The mean value increases to about 2 above the basin.

Basin Effects on Durations

Several ground-motion modeling studies have found that durations are significantly increased from 3D basin effects, in particular by the generation of surface waves at the basin edges (e.g., Vidale and Helmberger, 1988; Olsen *et al.,* 1995a,b). It is therefore important to understand to what extent the basin structure extends the ground-motion durations for the Los Angeles basin. In this section I compare the difference in duration between the 3D (model M3D) and 1D (model HK1D) simulations for the nine earthquake scenarios. As for the peak velocity computation, the source was identical in the 1D and 3D simulations for each scenario. The duration is measured as the cumulative time for which the vector ground velocity exceeds a threshold value (Tumarkin and Archuleta, 1997) of 5 cm/sec. Figure 10 shows the 3D-1D durations for the nine scenarios. Note that unlike the peak velocity ratios shown in Figures 6 to 9, the durations are directly related to the magnitude of the simulated earthquakes. The magnitude dependence is shown by a rela-

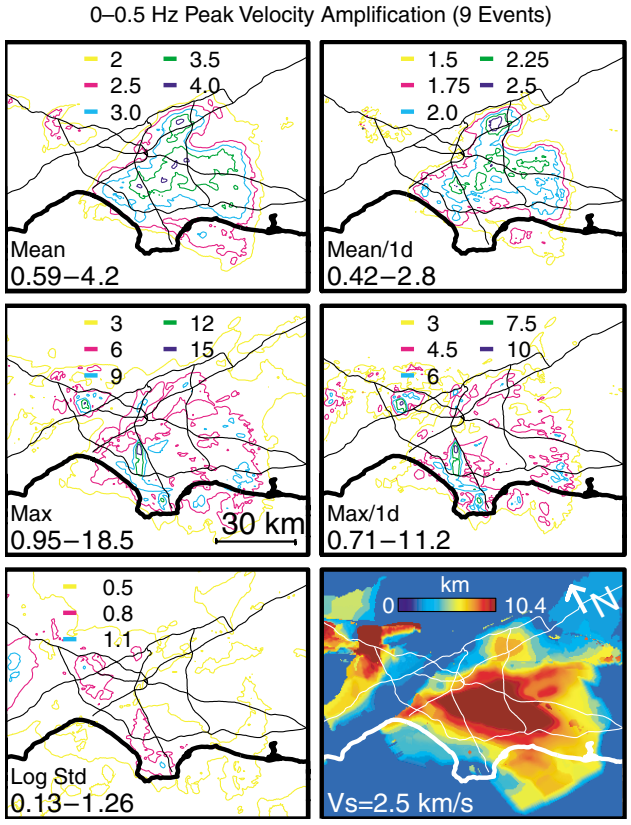

Figure 7. Maps of the 3D/1D 0–0.5 Hz peak velocity ratios and their uncertainties. Mean values without (top left) and with (top right) correction for 1D vertical *SH*-wave amplification, the maximum values without (middle left) and with (middle right) correction for 1D vertical SH-wave amplification, and the standard deviation of the natural log of the amplification (bottom left). The thin lines show major freeways in the area. The bottom right figure shows the isosurface for an *S*-wave velocity of 2.5 km/sec.

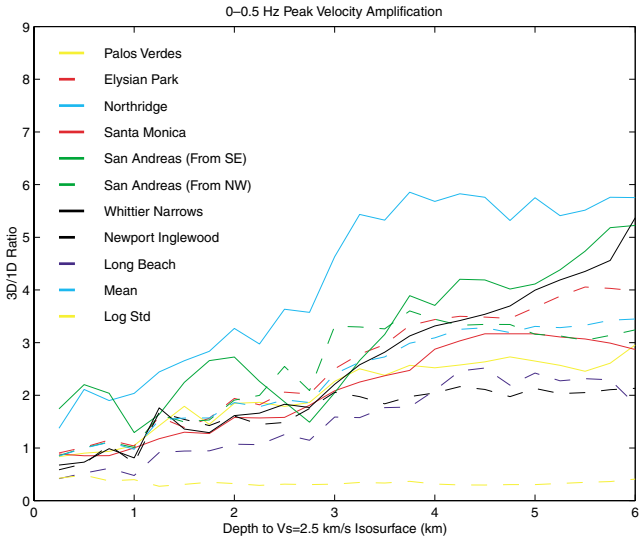

Figure 8. 3D/1D 0–0.5 Hz peak velocity ratios for the 9 scenarios shown in Figure 6, as well as their mean and log standard deviation, averaged for sites with common depth to the isosurface for an *S*-wave velocity of 2.5 km/sec.

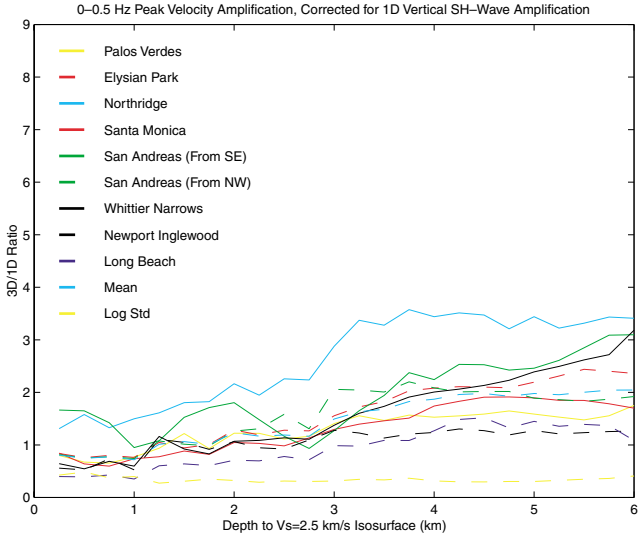

Figure 9. Same as Figure 7, but divided by the 1D vertical *SH*-wave amplification (Fig. 5).

tive large area affected by the 3D-1D durations for the SAF scenarios compared to some of those for the smaller events. The amplification south and west of the basin for the SAF scenario is a result of predominantly southward and westward propagating surface waves generated by the wavefield impinging onto the basin structure from the northwest and northeast. However, the areas affected by and maximum 3D-1D durations for the **M** 6.7 NR scenario are comparable to those for the larger SAF events. These results show, in addition to the effects of earthquake size and directivity, the importance of the fault proximity to the basin structure.

Accuracy and Limitations of Basin Amplification Results

Comparison to Data

Strong-motion recordings from the 1994 **M** 6.7 Northridge and 1987 **M** 5.9 Whittier-Narrows earthquakes are available for comparison with the simulations to examine the accuracy of the 3D modeling obtained in this study. Unfortunately, only the Northridge recordings have sufficient signal-to-noise ratio for frequencies below 0.5 Hz.

Figure 11 shows a comparison between 0.1–0.5 Hz data and synthetics for 11 stations representing various azimuths and distances from the causative fault. For each station, the comparisons are made at the same scale for all three components and for the available record length of the data. The fits among the phases vary considerably. The best results are obtained for stations located near the source, such as SSA

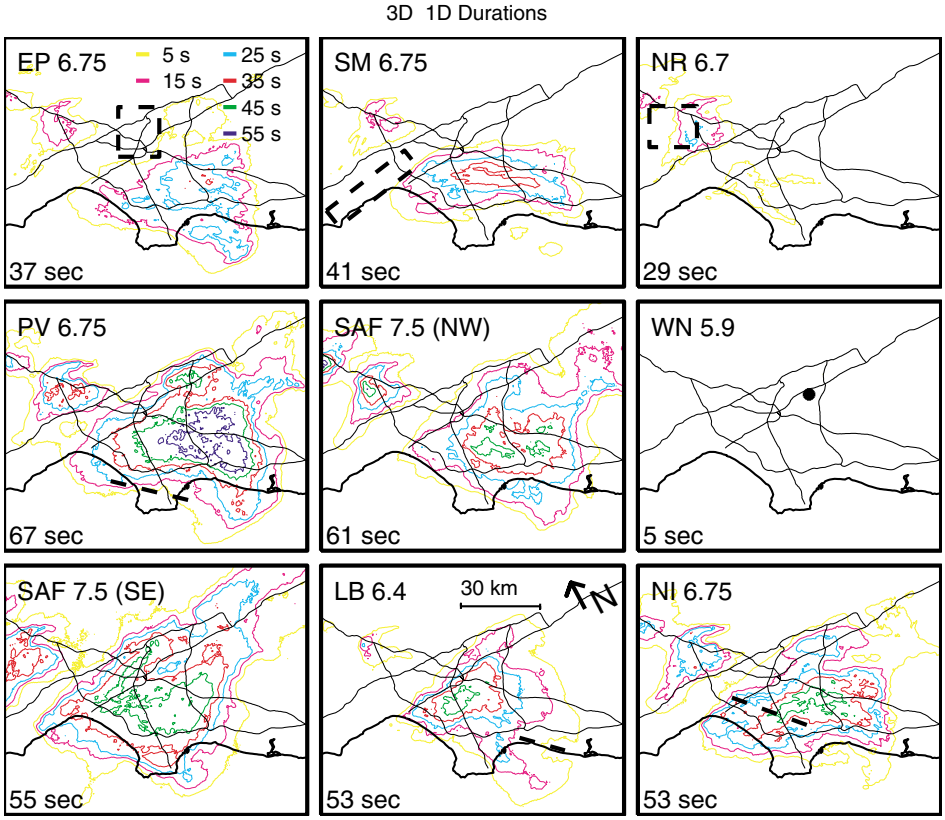

Figure 10. Maps of the 3D-1D durations for the nine scenarios shown in Figure 6. The thin lines show major freeways in the Los Angeles area and the thick line depicts the coastline. The range of the 3D-1D durations are listed for each scenario.

(Santa Susanna) and JFP (Jensen Filtration Plant). The fits are degraded near the Santa Monica Mountains and at large distances from the fault. The duration and amplitude of data and synthetics agree relatively well.

Figure 12 compares average horizontal 0.1–0.5 Hz peak velocities from the Northridge simulation at 59 sites in the LA basins to those computed from data. Almost all of the peak velocities are fit within a factor of 2 within this frequency range. The residuals are generally small above the basin, suggesting that the strength of anelastic attenuation used in the simulation was appropriate. The log standard deviation of the residuals for the 59 sites is 0.36, a reduction of 54% and 51% compared to the values obtained for the regional (HK1D) model and a 1D model defined by the velocity and density profile below the strong motion site DOW in the middle of the LA basin, respectively. This result suggests that long-period ground motion estimation can be improved considerably by including the 3D basin structure.

Omission of Low Velocities

I realize that the minimum velocity of 1 km/sec used in the simulations is unrealistically high for the basin sediments. In fact, the isosurface for $V_s = 1$ km/sec extends to a maximum depth of 1.3 km in the center of the LA basin. However, it is presently not feasible to include considerably lower velocities in the simulations with a maximum resolved frequency of 0.5 Hz. I therefore leave this important task for future work.

Reference Model

The 1D corrections were based on a smooth version of the regional model of Hadley and Kanamori (1977), which does not include the lower basin-sediment seismic velocities. One could also use the velocity profile below each site as the 1D reference model, an approach where the layering may cause pronounced wave guides. In order to examine the extent of such wave guide effects, I calculated the normalizing ground motion for Northridge using a plane-layered structure defined by the velocity profile at Downey (a deep sediment site in the center of the LA basin), with the source defined as in the M3D and HK1D models. Using the peak velocities at Downey from this simulation as the normalizing ground motion for that obtained from the 3D model decreased the amplification by 36% to 2.8 from the factor of 3.8 obtained at Downey in Figure 6. These results suggest that wave-guide effects can account for significant amplification. However, inclusion of the wave-guide effects would require separate calculations for each basin site, a task currently unrealistic due to computer limitations.

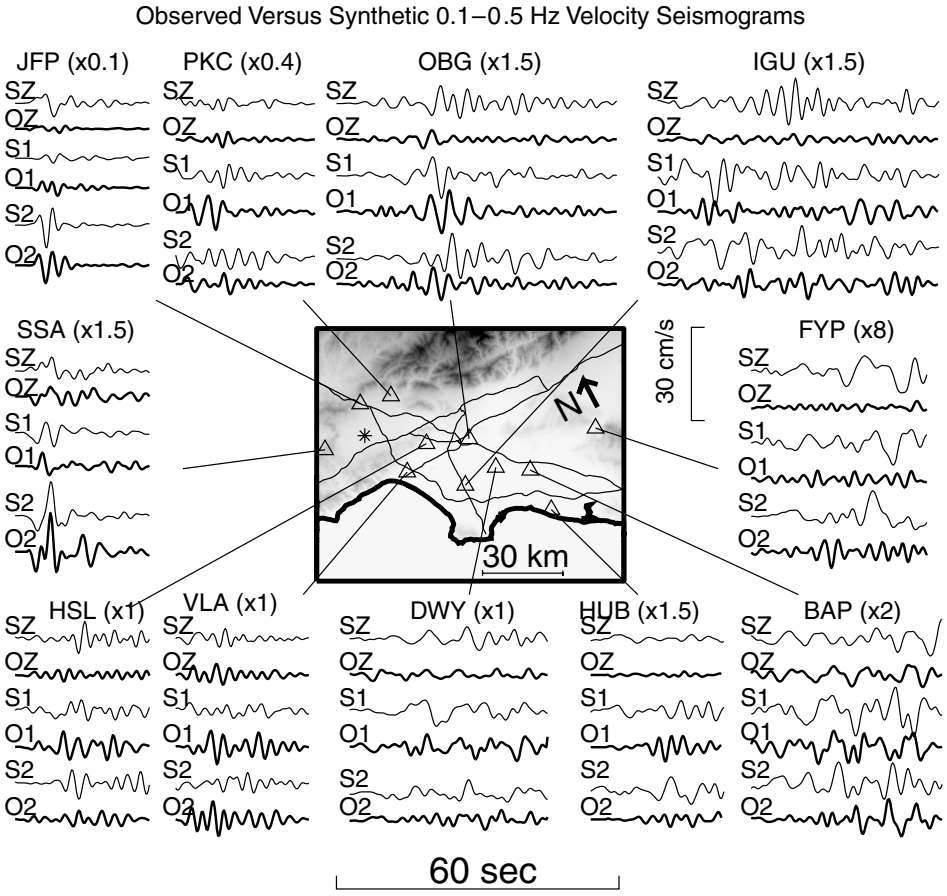

Figure 11. Comparison of observed versus synthetic 0.1–0.5 Hz waveforms at 11 sites within the model. O and S depict observed (thick traces) and synthetic (thin traces) seismograms, respectively, and Z, 1, and 2 depict vertical, 118°, and 28° horizontal components, respectively.

Number of Scenarios

The main limitations of the average amplification map for Los Angeles result from the relatively small number of scenario earthquakes (nine) and their maximum frequency (0.5 Hz) used for its construction. It will be important to incorporate more simulations of geologically reasonable scenarios in order to reduce the uncertainty of the average ratios, and to increase the highest frequencies to capture the entire spectrum of amplification effects. Unfortunately, both of these tasks are limited by the large computational requirements for the simulations. However, considering the recent explosive increase in computational power, it may be feasible to construct more accurate and reliable amplification maps in the near future. These maps should include the effects of realistic rupture parameters and anelastic attenuation as well.

Conclusions

I have used 3D/1D 0–0.5 Hz peak velocity ratios to construct site amplification maps for the Los Angeles basin for nine earthquake scenarios (**M** 6.75 earthquakes on the Palos Verdes, Elysian Park, Santa Monica, Newport-Inglewood faults, approximations to the **M** 6.7 1994 Northridge, the **M** 6.4 1933 Long Beach, and the **M** 5.9 1987 Whittier-Narrows events, and two **M** 7.5 earthquakes on a 170-km long stretch of the San Andreas fault). The individual scenarios show amplification of peak velocities up to an order of magnitude relative to the background model. The distribution of mean peak velocity ratios, as calculated from the nine scenarios, has a maximum of 4.2. In general, both the individual scenarios and their mean values show that the largest amplifications occur above the deepest parts of the basin and above the steeply-dipping basin boundaries. The largest mean amplification is furthermore associated with relatively small uncertainties. The largest uncertainties of the mean amplification above the basin (log standard deviation > 1.1) are associated with sites on Palos Verdes, in the southern part of SFV, and northwest of SFV. For the nine scenario earthquakes, the amplification tends to increase with distance from the causative fault to the basin structure. It is possible that this pattern is due to stronger amplification of the more complex wavefield impinging onto the basin

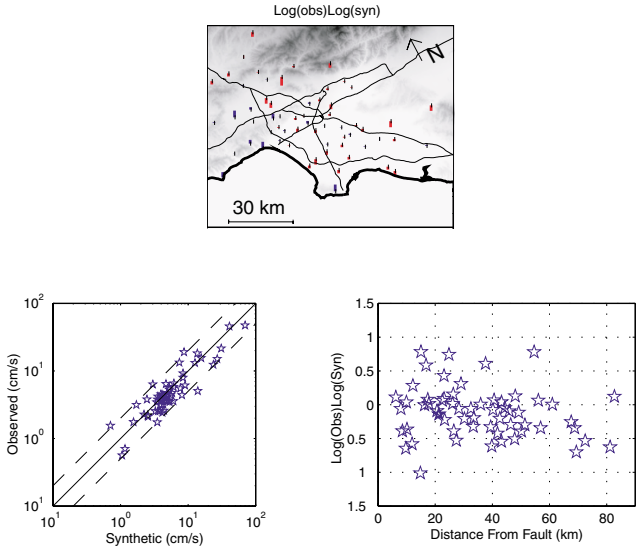

Figure 12. Comparison of observed versus synthetic 0.1–0.5 Hz peak velocities for 59 sites in the Los Angeles area for the 1994 Northridge earthquake. *Top* Difference between the log of the observed and synthetic peak velocities at each of the 59 sites, represented by the length of the bars; blue depicts underprediction, red depicts overprediction. *Bottom left:* Observed versus synthetic peak velocities. The dashed lines represent factor-of-two discrepancies. *Right:* Difference between the natural log of the observed and synthetic peak velocities versus distance from the fault.

structure from the distant earthquakes compared to that of the predominant body waves from nearby earthquakes. The amplification is caused by a combination of effects from the 3D basin structure and differences in impedance between the 1D and 3D models. As an estimate of the latter, 1D vertical *SH*-wave amplification in profiles of the 3D model accounts for amplifications of up to 1.7 above the basins. After correction for this effect, the maximum amplification averaged over sites above similar basin structure for the scenario earthquakes is 6.5, associated with sites located above the deeper part of the basin. Durations are significantly increased by the 3D basin structure. Compared to the smaller earthquakes, the **M** 7.5 San Andreas events generate extended durations over a much larger area, particularly above and beyond the southern, eastern, and western parts of the basin. The largest 3D–1D durations are obtained for the Palos Verdes (67 sec), Long Beach (53 sec), Newport-Inglewood (53 sec), and San Andreas (55/61 sec) earthquakes, for basin sites.

I used the simulation of the 1994 Northridge earthquake to validate the amplification results for the LA basin. The 0–0.5 Hz synthetic seismograms are in satisfactory agreement with data, in particular at near-source stations. In addition, the discrepancy between synthetic and observed peak velocities is less than a factor two at most sites and the log standard deviation of the residuals is 0.36. This value represents a reduction of 54% and 51% compared to the values obtained for the regional 1D model (HK1D) and a 1D model defined by the velocity and density profiles below site DOW in the middle of the basin, respectively. Thus, the results for Northridge suggest that estimation of long-period ground motion can be improved considerably by including the 3D basin structure in the modeling.

Acknowledgments

The computations in this study were carried out on SGI Origin 2000 computers at MRL, at University of California, Santa Barbara (NSF Grant CDA96-01954) and Los Alamos National Laboratories, with support from NSF Grant EAR 96-28682 and the Southern California Earthquake Center (SCEC). SCEC is funded by NSF Cooperative Agreement EAR-8920136 and USGS Cooperative Agreements 14-08-0001-A0899 and 1434-HQ-97AG01718. This manuscript has been improved by careful reviews by Steve Day, Ned Field, and an anonymous reviewer and from useful comments by Norm Abrahamson, Paul Somerville, Jamie Steidl, Ralph Archuleta, and Alexei Tumarkin. This is SCEC contribution 546 and Institute for Crustal Studies Contribution 0335-87EQ.

References

Blanch, J. O., J. O. A. Robertsson, and W. W. Symes (1995). Modeling of a constant Q: methodology and algorithm for an efficient and optimally inexpensive viscoelastic technique, *Geophysics* **60,** 176–184.

Cerjan, C., D. Kosloff, R. Kosloff, and M. Reshef (1985). A nonreflecting boundary condition for discrete acoustic and elastic wave equations, *Geophysics* **50,** 705–708.

Clayton, R., and B. Engquist (1977). Absorbing boundary conditions for acoustic and elastic wave equations, *Bull. Seism. Soc. Am.* **67,** 1529–1540.

Dolan, J. J., K. Sieh, T. K. Rockwell, R. S. Yeats, J. Shaw, J. Suppe, G. J. Huftile, and E. M. Gath (1995). Prospects for larger or more frequent earthquakes in the Los Angeles Metropolitan region, *Science* **267,** 199–205.

Faust, L. Y. (1951). Seismic velocity as a function of depth and geologic time, *Geophysics* **16,** 192–206.

Frankel, A. (1993). Three dimensional simulations of ground motions in the San Bernardino Valley, California, for hypothetical earthquakes on the San Andreas Fault, *Bull. Seism. Soc. Am.* **83,** 1042–1063.

Frankel, A., and J. Vidale (1992). A three-dimensional simulation of seismic waves in the Santa Clara Valley, California, from a Loma Prieta aftershock, *Bull. Seism. Soc. Am.* **82,** 2045–2074.

Graves, R. W. (1995). Preliminary analysis of long-period basin response in the Los Angeles region from the 1994 Northridge earthquake, *Geophys. Res. Lett.* **22,** 101–104.

Graves, R. W. (1996). Simulating seismic wave propagation in 3D elastic media using staggered-grid finite differences, *Bull. Seism. Soc. Am.* **86,** 1091–1106.

Hadley, D., and H. Kanamori (1977). Seismic structure of the Transverse Ranges, California, *Geol. Soc. Am. Bull.* **88,** 1469–1478.

Hough, S. E., C. Dietel, G. Glassmoyer, and E. Sembera (1995). On the variability of aftershock ground motions in the San Fernando Valley, *Geophys. Res. Lett.* **22,** 727–730.

Levander, A. R. (1988). Fourth-order finite-difference P-SV seismograms, *Geophysics* **53,** 1425–1436.

Ludwig, W. J., J. E. Nafe and C. L. Drake (1970). Seismic refraction, in *The Sea,* A. E. Maxwell (Editor), Vol. 4, Wiley-Interscience, New York, 53–84.

Magistrale, H., R. Graves, and R. Clayton (1998). A standard three-dimensional seismic velocity model for southern California: Version 1, *EOS Trans. AGU* **79,** F605.

Nafe, J. E. and C. L. Drake (1960). Physical properties of marine sediments, in *The Sea* M. N. Hill (Editor), Vol. 3, Wiley-Interscience, New York, 794–815.

Olsen, K. B. (1994). Simulation of three-dimensional wave propagation in the Salt Lake Basin, *Ph.D. Thesis,* University of Utah, Salt Lake City, Utah.

Olsen, K. B., and G. T. Schuster (1994). Three-dimensional modeling of site amplification in East Great Salt Lake Basin, U.S. Geological Survey Technical Report, 1434-93-G-2345, 102 p.

Olsen, K. B., and G. T. Schuster (1995). Causes of low-frequency ground motion amplification in the Salt Lake Basin: the case of the vertically-incident *P* wave, *Geophys. J. Int.* **122,** 1045–1061.

Olsen, K. B., and R. J., Archuleta (1996). Three-dimensional simulation of earthquakes on the Los Angeles Fault System, *Bull. Seism. Soc. Am.* **86,** 575–596.

Olsen, K. B., J. C. Pechmann, and G. T. Schuster (1995a). Simulation of 3-D elastic wave propagation in the Salt Lake Basin, *Bull. Seism. Soc. Am.* **85,** 1688–1710.

Olsen, K. B., R. J., Archuleta, and J. R. Matarese (1995b). Three-dimensional simulation of a magnitude 7.75 earthquake on the San Andreas fault in southern California, *Science* **270,** 1628–1632.

Robertsson, J. O. A., J. O. Blanch, and W. W. Symes (1994). Viscoelastic finite-difference modeling, *Geophysics* **59,** 1444–1456.

Scholler, B., K. McLaughlin, S. Day, and H. Magistrale (1994). 3D long period strong motion finite difference simulations in the LA basin. I. Numerical methods utilizing recursive grid refinement (abstract), *Seism. Res. Lett.* **65,** 39.

Tumarkin, A. G., and R. J. Archuleta (1997). Recent advances in prediction and processing of strong ground motions, *Natural Hazards* **15,** 2–3, 199–215.

Vidale, J. E., and D. V. Helmberger (1988). Elastic finite-difference modeling of the 1971 San Fernando, California, earthquake, *Bull. Seism. Soc. Am.* **78** 122–141.

Wald, D. J., and T. H. Heaton (1994). Spatial and temporal distribution of slip for the 28 June 1998 Landers, California, earthquake, *Bull. Seism. Soc. Am.* **84,** 668–691.

Wald, D. J., T. H. Heaton, and K. W. Hudnut (1996). The slip history of the 1994 Northridge, California, earthquake determined from strong motion, teleseismic, GPS, and levelling data, *Bull. Seism. Soc. Am.* **86,** S49–S70.

Yomogida, K., and J. T. Etgen (1993). 3-D wave propagation in the Los Angeles basin for the Whittier-Narrows earthquake, *Bull. Seism. Soc. Am.* **83,** 1325–1344.

Appendix

So far in this study, the assessment of the Los Angeles basin amplification effects has been carried out with little reference to the underlying physics of wave propagation. However, it is important to understand the mechanisms causing the spatially variable amplification in order to improve the ground-motion estimates in the future. This appendix contains a brief analysis of three-component 1D and 3D synthetic seismograms along a profile across the LA basin for the nine earthquake scenarios described earlier in the article. I also show snapshots to support the interpretation of the wave propagation for three selected events, the Newport-Inglewood (NI), Northridge (NR), and San Andreas from southeast (SAFS). The identification of the phases is aided by particle-motion analysis.

Figures A.1–A.3 show 3D and 1D synthetic seismograms along the profile shown in Figure 3 for the nine scenarios. The profile is selected to intersect the deepest part of the LA basin, and it is located above some of the sites representing the largest amplification in the model area (see Figure 6 and 7). In particular, the profile is located near the peaks in amplification obtained in the San Gabriel Valley and the main trough of the LA basin. The synthetics are scaled by the same factor for each component for each scenario, but by different factors between the scenarios. The distance measures used in the following discussion refer to those shown in Figures A.1–A.3.

The differences between the 3D and 1D seismograms explain the genesis of some of the strong basin effects described in earlier sections, and help separate the basin effects from those due to geometrical spreading. Typically, the 1D seismograms contain only the direct arrivals from the source, while secondary arrivals due to phenomena such as surface wave generation and resonances can be seen in the 3D traces. Compared to the 1D traces, the 3D seismograms are generally characterized by much prolonged duration, as shown in Figure 10.

Elysian Park (EP)

The main feature of the 1D traces for EP is the direct *S* wave on all components, strongest on the vertical, with a phase shift near 50 km from the source radiation pattern. Part of the energy of the direct arrival is converted to secondary arrivals with extended durations in the 3D synthetics. A Love wave is generated near the north-northwestern boundary of the main trough and propagates toward the south. A secondary phase with lower predominant frequency on the 118° and vertical components is generated in the center of the basin (30–50 km). Note that this secondary phase is most energetic above the steeply dipping southwestern flank of the trough (35 km).

Santa Monica (SM)

Similar to EP, the thrust rupture for SM generates considerable energy on the vertical component, directed into the LA basin trough (energetic 1D arrivals at 10–50 km). This energy is amplified between 30 and 50 km in the 3D model, and the duration is much prolonged by dispersive surface waves, in part Rayleigh waves. These surface waves are, among other directions, propagating southwest from the northern boundary of the trough (50 km). The largest amplitude of these phases appear towards the center of the basin (35–45 km).

Long Beach (LB)

This relatively small event caused the smallest maximum amplification among the scenarios. The mostly horizontal energy from the rupture is seen to propagate towards northeast on the 118° component. Note the surface (Love)

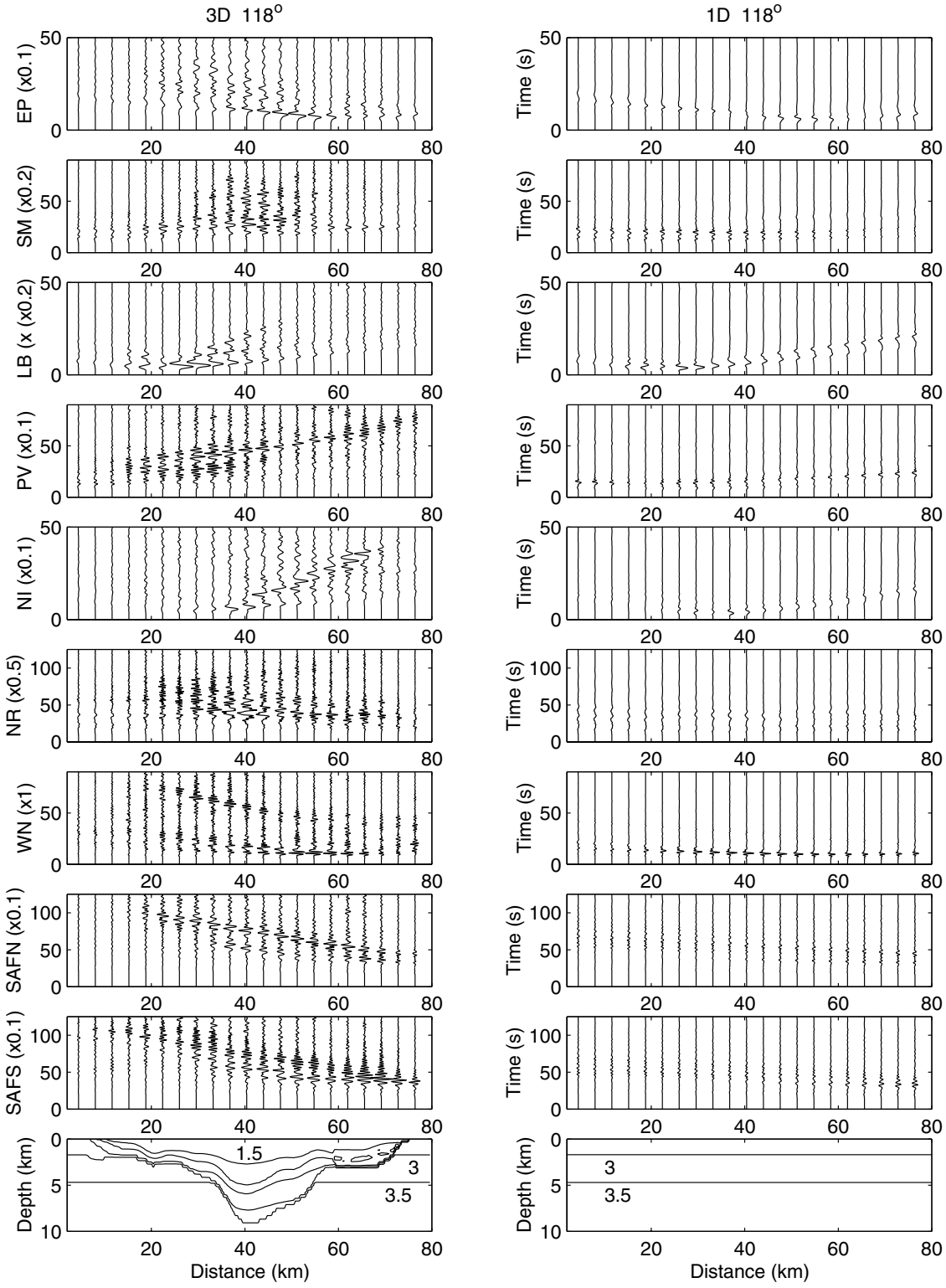

Figure A.1. 118° 3D and 1D synthetic seismograms for each of the nine scenarios along the profile shown in Figure 3. The traces are scaled by the same factor for the different components for each scenario, but a different factor (listed in the label) among the scenarios. The bottom panels show cross sections of the 3D and 1D models along the profile. Contours (some labeled) vary between 1.5 km/sec and 3.5 km/sec with a spacing of 0.5 km/sec.

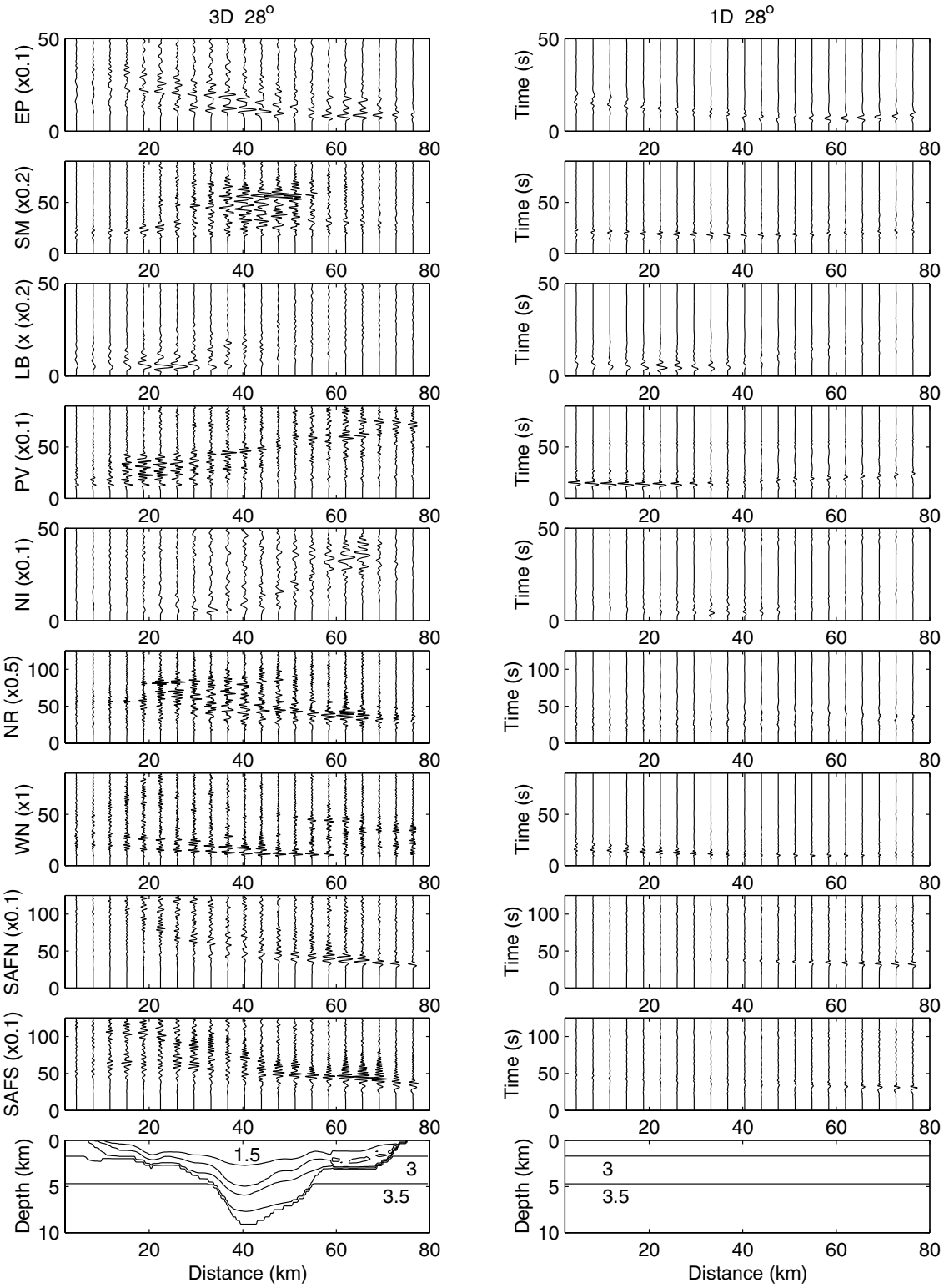

Figure A.2. Same as Figure A.1, but for 28°.

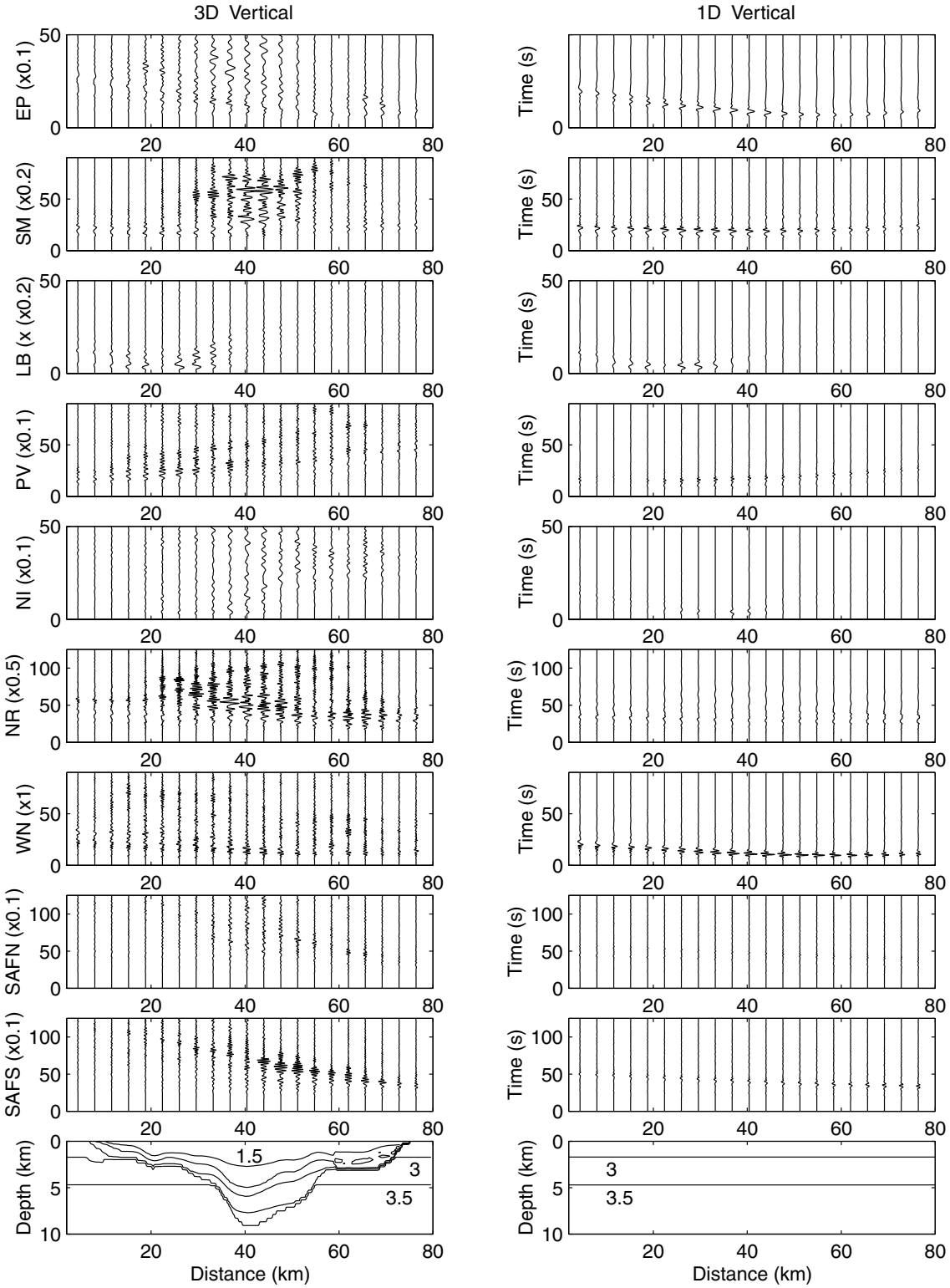

Figure A.3. Same as Figure A.1, but for the vertical component.

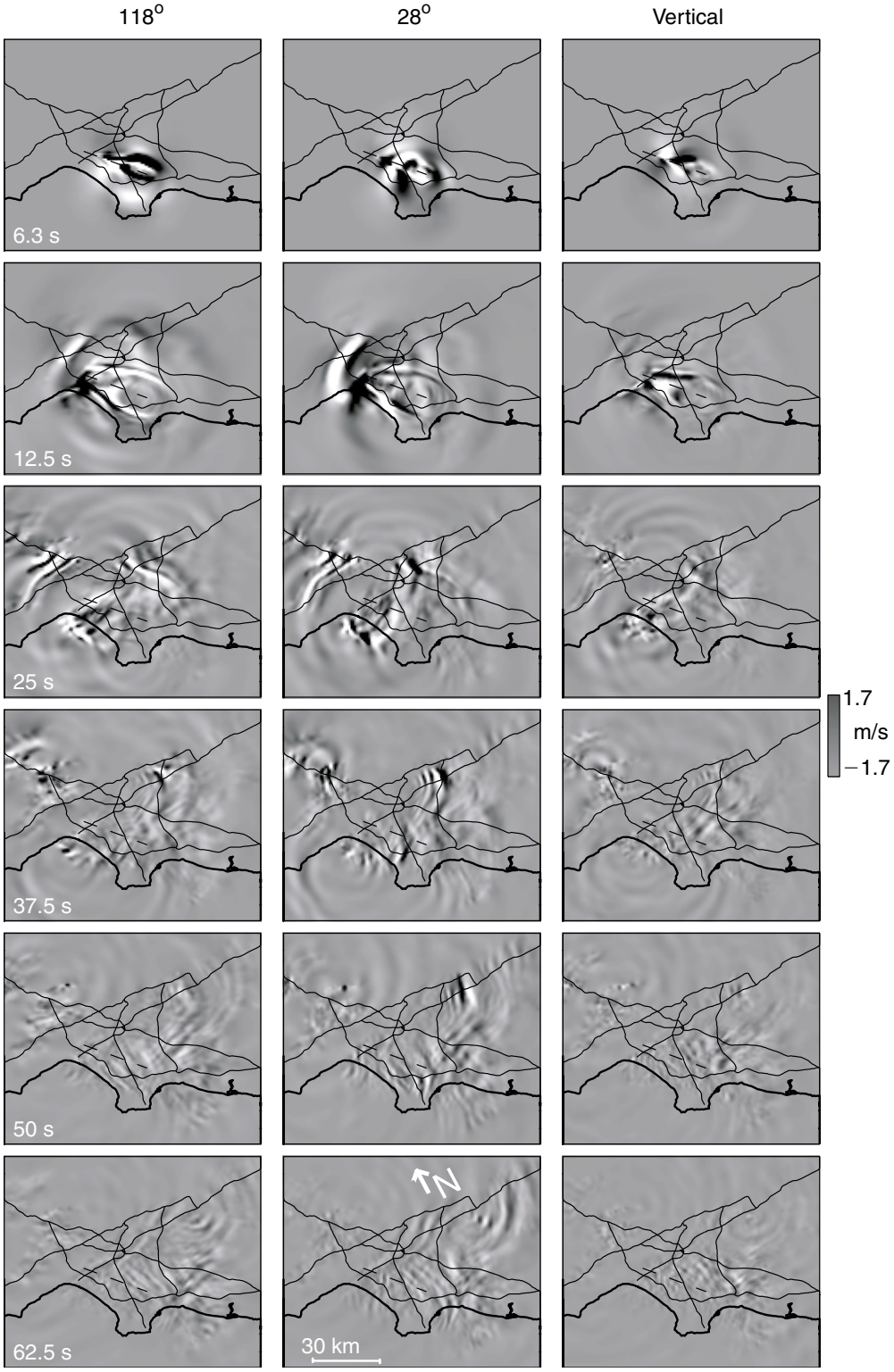

Figure A.4. Snapshots of simulated wave propagation in the Los Angeles area for NI along 118°, 28°, and vertical from 6.25 to 75 s after the origin time of the rupture. Light (dark) shading depicts negative (positive) particle velocity. The particle motion is scaled by a constant for all snapshots. The dashed line depicts the surface fault trace. The thin lines show major freeways in the Los Angeles area.

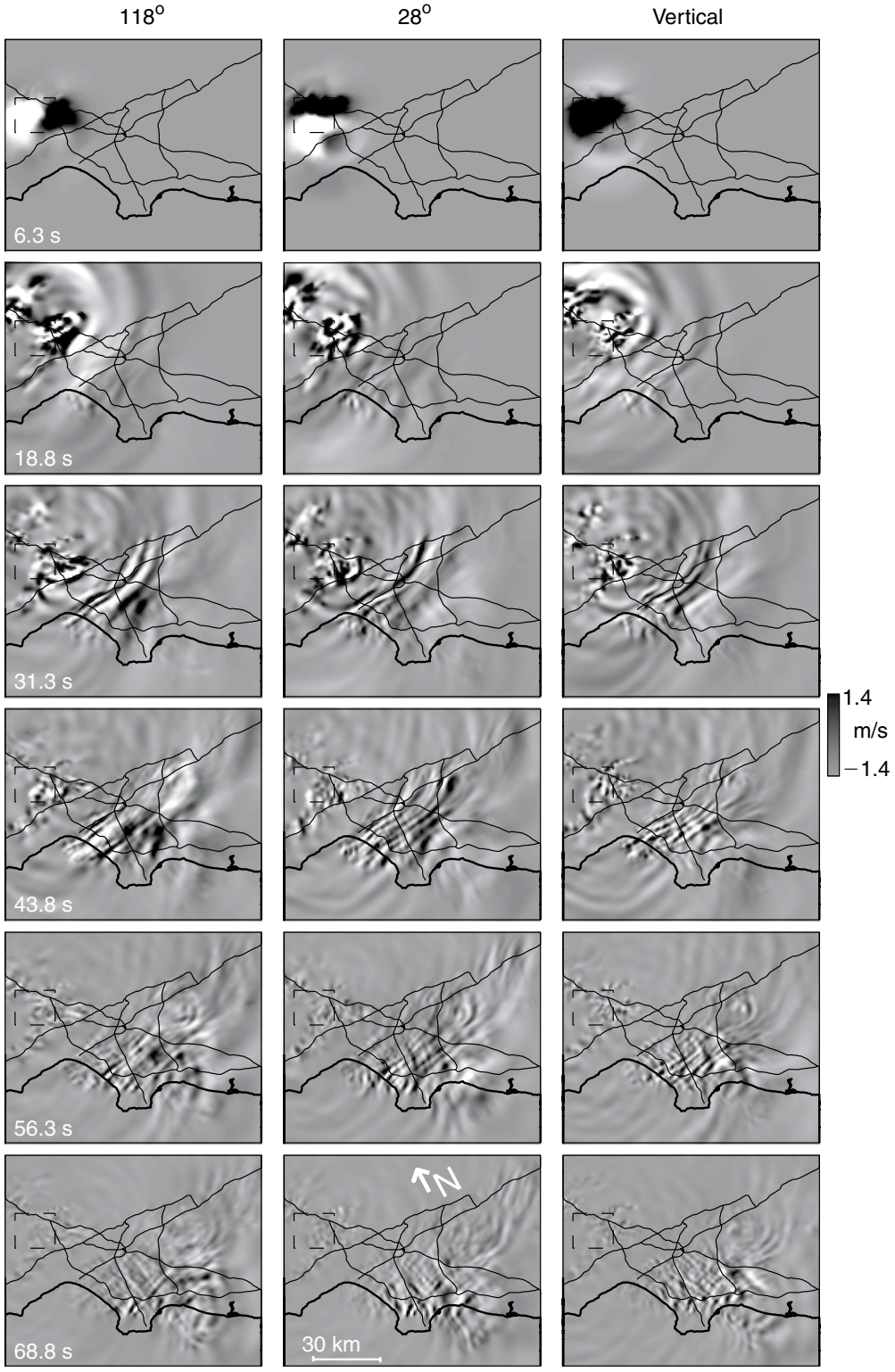

Figure A.5. Same as Figure A.4, but for NR.

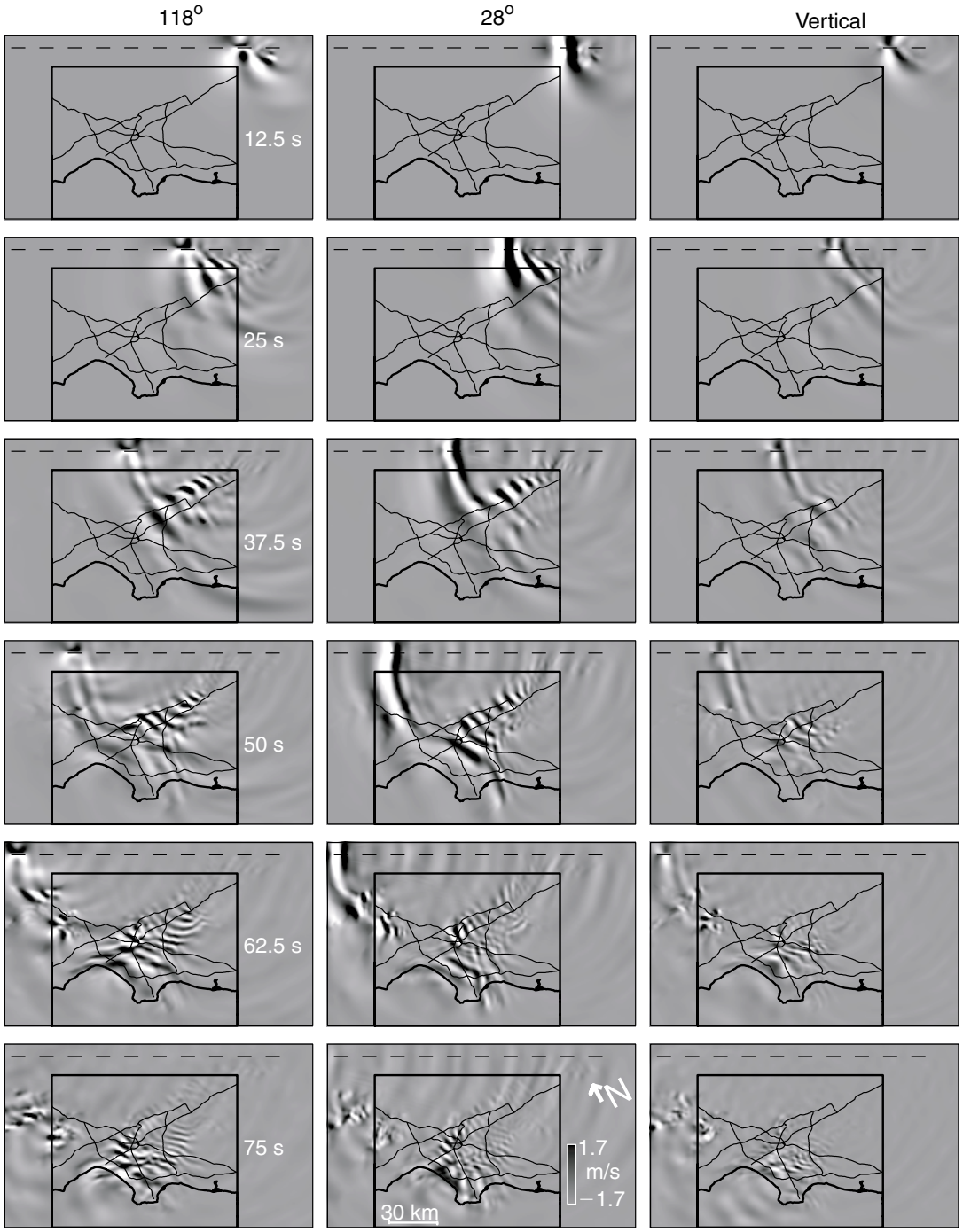

Figure A.6. Same as Figure A.4, but for SAFS.

waves generated near the fault (25 km), propagating southwest and particularly northeast toward the deepening basin. Also note how the 1D amplitudes are stronger than the 3D ones, northeast from about 50 km, causing deamplification for basin depths less than about 2 km in Figures 6–7. This is due to transfer of energy from the initial to secondary phases caused by basin effects in the 3D model.

Palos Verdes (PV)

This strike-slip event generates predominantly horizontal energy, which along the profile is strongest near the fault on the 28° component. Strong reverberating energy appear in the shallow southwestern end of the basin along 118°. A Love wave generated at the steeply dipping flank propagates toward northwest which, in turn, reflects back in southern

directions, in particular on the 28° component, after about 70 sec. As for LB, PV generates deamplification in the southern part of the basin (compare 1D and 3D on the 28° component).

Newport-Inglewood (NI)

The northwest-southeast trending strike-slip fault responsible for the NI scenario is located along the southwestern slope of the LA basin trough. The northwest-propagating rupture and the fault geometry is favorable for direction of energy toward northwest and northeast (see snapshots in Figure A.4, at 6.25–25 sec). Note how the predominantly northeast-propagating *SH*/Love-wave (40–70 km on 118° in Figure A.1) generates strong resonance on the 28° component in the San Gabriel Valley (SGV) (60–70 km). The snapshots at 25 sec and later times explain this transfer of energy: the northeast-propagating phase with predominant transverse motion is redirected toward east-southeast by the shallowing sediments in SGV. The part of the energy directed towards northwest generates resonance in the deepest part of SFV near the I5/I405 intersection (see snapshots at 25 sec and later). *SH*/Love wave energy is generated close to the I10/I405 intersection near the basin edge, which propagates toward southeast along the I405 (snapshots, in particular 28°, at 25 sec and later).

Northridge (NR)

The simulation of the 1994 Northridge event generated the largest amplification among the nine scenarios covering the widest area (see Figure 6). The strong amplification is shown by the large differences between the 3D and 1D synthetics in Figures A.1–A.3. The amplitude is comparably large on all components of the 3D traces with much extended durations in some areas. The 28° and vertical components show strong resonance in the San Gabriel Valley (60–70 km). Surface waves are generated at both southwestern and northeastern boundaries of the trough (20 and 50 km), producing a criss-cross pattern in the LA basin by refraction and reflection at the basin boundaries (see snapshots in Figure A.5 at 31 sec and later). The surface waves include a large-amplitude Rayleigh wave generated just south of the Santa Monica Mountains after the wavefield has entered the LA basin (seismograms at 35–50 km and snapshots in Figure A.5 at 31.3 s and later).

Whittier-Narrows (WN)

This scenario generated deamplification for sites with depths less than about 1 km (see Figures 8–9), as indicated by the larger amplitude on the 1D traces compared to those in the 3D synthetics. *SH*/Love waves are generated near the northeastern boundary of the trough at about 10 sec and 40 sec (118°), propagating toward northeast and particularly southwest. Resonance is seen in the SGV on the 28° component.

San Andreas (SAFN and SAFS)

The strike-slip SAF scenarios generate predominantly *SH* energy, with the 28° component amplified near the fault due to directivity effects, as pointed out by Olsen *et al.* (1995b). The much extended duration here is due not only to basin effects, but also the rupture duration in excess of 60 sec. A Love wave with southerly propagation direction and particularly strong dispersion for SAFS is generated when the wavefields enter the SGV, causing increased amplification at 55–70 km on the 28° component. Resonance is generated in the LA basin between at 40–60 km (see also snapshots in Figure A.6, 50 sec and later), where the particle motion differs from that of a Rayleigh wave. The Love waves are amplified (see Figure 6) upon striking the southern boundary of the basin (25–35 km on the 118° component).

Institute for Crustal Studies
UCSB, Santa Barbara, CA 93106-1100

Manuscript received 1 July 2000.